Nanoscale

ROYAL SOCIETY OF CHEMISTRY

PAPER

View Article Online
View Journal | View Issue

Cite this: *Nanoscale*, 2025, **17**, 9184

Programming a multiplex lanthanide nanoparticle for customized cancer treatment with real-time efficiency feedback†

Hongxia Zhao,[a,d] Wei Chen,[b] Yu Zhu,[a] Zhicong Chao,[a] Jiahui Sun,[a] Qing Zhang,[b] Hongqian Guo,[b] Huangxian Ju [a] and Ying Liu *[a,c]

Customized cancer therapy relies on timely therapeutic effect evaluation to provide prescription adjustment for individual cases. However, currently reported therapeutic reagents are rarely integrated with imaging probes for self-evaluation of effects. Contrast imaging agents to measure tumor size changes must be administrated separately after therapy, complicating the therapeutic process and delaying reporting time. Herein, we design a customized therapy platform (LNPs-RB/Pep/cRGD) by conjugating lanthanide nanoparticles (LNPs) with the photosensitizer rose bengal, a caspase-3 substrate peptide (with Cy7.5 labelled at the terminal), and the tumor-targeting molecule cRGD. LNPs exhibit NIR-IIb downconversion luminescence under 980 nm/808 nm excitations for *in vivo* imaging, and visible upconversion luminescence under high-power 980 nm excitation for photodynamic therapy (PDT). By sequentially programming NIR excitation wavelength and power, NIR-IIb-imaging guided PDT and real-time cancer cell apoptosis imaging are achieved as therapeutic efficiency feedback. PDT induces cell apoptosis, generating caspase-3, which cleaves Cy7.5-containing peptide fragments from LNPs. This process corresponds to a recovery *in vivo* of NIR-IIb ratiometric imaging at 808 nm *versus* 980 nm excitation. The cleaved Cy7.5-containing peptide fragment is cleared into urine for NIR imaging. Both cell apoptosis imaging processes are completed 12 h after PDT, which is 7 days earlier than tumor size measurement. Therefore, customized therapy is achieved by timely adjusting PDT dosage, enhancing therapeutic efficacy.

Received 27th January 2025,
Accepted 10th March 2025

DOI: 10.1039/d5nr00390c

rsc.li/nanoscale

1. Introduction

The dynamic progression of tumor development and individual heterogeneity among cancer patients affect therapeutic efficacy.[1–3] Customized cancer treatment relies on real-time efficiency feedback, enabling timely prescription adjustments for individual cases and, correspondingly, enhancing therapeutic efficiency while reducing overtreatment or side effects.[4–6] However, current therapeutic evaluation techniques are mainly executed post-treatment, measuring tumor volumetric changes through magnetic resonance imaging (MRI), computed tomography (CT), positron emission tomography (PET), or biopsy examinations, which are either delayed in reporting or require invasive sampling processes.[7–9] Additionally, "post-treatment" evaluations typically require repeated dosing of contrast agents after treatment, complicating the process.[10] Customized cancer therapy that integrates treatment and *in situ* therapeutic efficacy evaluation methodologies into a single system has not been reported.

Three components must be integrated to develop a customized cancer treatment system: a drug molecule for therapeutic exertion, an imaging probe for real-time reporting of cell apoptosis, and an "internal standard" probe for signal self-calibration to eliminate changes in probe concentration due to accumulation or metabolism during *in vivo* experiments. Caspase-3 protease is a crucial mediator of apoptosis[11–13] and serves as a classical molecular marker for cell apoptosis. Currently reported caspase-3 imaging principles mainly rely on regulating intramolecular charge transfer (ICT) processes[14] or fluorescence resonance energy transfer (FRET) processes[15,16] between a fluorescent dye and its corresponding quencher labelled to the caspase-3 substrate peptide. However, the detection windows are typically confined to the visible

[a]*State Key Laboratory of Analytical Chemistry for Life Science, School of Chemistry and Chemical Engineering, Nanjing University, Nanjing 210023, China. E-mail: yingliu@nju.edu.cn*
[b]*Department of Urology, Affiliated Drum Tower Hospital, Medical School of Nanjing University, Institute of Urology, Nan-jing University, Nanjing 210023, China*
[c]*Chemistry and Biomedicine Innovation Center, Nanjing University, Nanjing 210023, China*
[d]*College of Pharmacy and Chemistry & Chemical Engineering, Taizhou University, Jiangsu, Taizhou 225300, China*

† Electronic supplementary information (ESI) available. See DOI: https://doi.org/10.1039/d5nr00390c

range (Vis, 400–700 nm)[17–20] and the first near-infrared (NIR-I, 700–950 nm) window.[14,21] Conversely, few detection systems extend into the second near-infrared (NIR-II, 1000–1700 nm) window,[15] especially the NIR-IIb (1500–1700 nm) window, which provides deeper penetration, higher spatial resolution, and lower photon scattering.[22,23] Red-shifting the emission wavelength of caspase-3 reporting probe dye is difficult because it requires π-extension and heterocyclic modification of the organic dye skeleton, leading to reporter dye aggregation and fluorescence quenching in polar solvents.[24,25] Furthermore, conjugating the caspase-3 reporting probe dye with an extra "internal standard" dye or drug molecule requires extra connector design and complicates the synthesis process, making accurate evaluation of the therapeutic effect difficult.

Lanthanide nanoparticles (LNPs) produce tunable multicolor luminescences from the upconversion UV/visible region to the downconversion NIR-II region under different NIR excitations,[26–31] making them ideal candidates for developing a customized therapeutic platform with real-time efficiency feedback.[32,33] Activatable LNP probes in the NIR-IIb region have been reported for oxidative and reductive small molecules, such as reactive oxygen species (ROS),[34,35] ClO^-,[36] $ONOO^-$,[37] GSH.[38,39] However, LNP-based NIR-IIb imaging of the protease caspase-3, a molecular marker directly related to therapy efficiency, has not been reported. Here, we reported a multiplex LNP and programmed its NIR-IIb downconversion luminescence and visible upconversion luminescence to achieve customized cancer therapy by using *in vivo* caspase-3 responsive downconversion NIR-IIb imaging as real-time efficiency feedback to guide the duration of photodynamic therapy (PDT). The LNPs consist of a luminescence core ($NaGdF_4$:Yb,Er,Ce) to generate downconversion emission at 1550 nm and upconversion emission at 542/650 nm, a NIR absorption shell ($NaYbF_4$:Nd) to absorb NIR excitations at 980/808 nm, and an inert shell ($NaGdF_4$) to minimize surface defects for luminescence enhancement (Scheme 1a, LNPs). The LNPs surface is functionalized with amphiphilic polymer, DSPE-PEG/DSPE-PEG-cRGD, to target cancer cell surface receptor $\alpha_v\beta_3$ integrin, and DSPE-PEG-DBCO to connect caspase-3 substrate peptide. The photosensitizer, rose bengal (RB), is loaded on the LNP surface *via* hydrophobic–hydrophobic interaction with DSPE to perform PDT. The caspase-3 protease substrate peptide, labelled with N_3 and Cy7.5 (N_3-Pep-Cy7.5), is covalently modified on the LNP surface (DSPE-PEG-DBCO) *via* click chemistry to achieve real-time efficiency feedback (Scheme 1a, LNPs-RB/Pep/cRGD). Cy7.5 serves as an efficient photon filter for the LNPs' 808 nm excitation energy, causing notable quenching of the LNPs' 1550 nm emission under 808 nm excitation, while not affecting its 1550 nm emission under 980 nm excitation.

NIR-IIb emission of LNPs-RB/Pep/cRGD under low-power 980 nm excitation navigates its delivery in the systemic circulation, clearly indicating tumor location and appropriate timing for performing PDT (Scheme 1b, NIR-IIb navigation). PDT is performed under high-power 980 nm excitation to produce ROS for cancer cell apoptosis (Scheme 1b, PDT execution). Activated caspase-3 within apoptotic cells then cleaves its substrate peptide and releases the Cy7.5-containing peptide fragment, which recovers the NIR-IIb emission of LNPs under 808 nm excitation. Real-time therapeutic efficiency feedback is achieved by evaluating NIR-IIb ratiometric imaging ($F_{1550,\ Ex808}/F_{1550,\ Ex980}$) *in situ* at the tumor location. Meanwhile, the cleaved Cy7.5-containing peptide fragment is metabolized to urine by renal clearance, which shows fluorescence over 900 nm and enables urine imaging as an extra evaluation mode for therapeutic efficiency feedback (Scheme 1b, real-time efficiency feedback). Both *in vivo* NIR-IIb fluorescence imaging and urine NIR fluorescence report cell apoptosis 12 h after PDT execution, serving as early evaluation of therapeutic efficiency, which is ~1 week earlier compared to imaging tumor size change. Customized therapeutic plan adjustments are timely performed according to caspase-3 real-time imaging results (Scheme 1b, customized treatment), effectively improving *in vivo* therapeutic efficiency.

2. Results and discussion

2.1. Synthesis of LNPs-RB/Pep and characterization of ROS generation and caspase-3 response

LNPs $NaGdF_4$:Yb,Er,Ce@$NaYbF_4$:Nd@$NaGdF_4$ were synthesized *via* a co-precipitation method, composed of a luminescence core, $NaGdF_4$:Yb,Er,Ce, the 980/808 nm NIR absorption shell, $NaYbF_4$:Nd, and inert shell, $NaGdF_4$ (Scheme 1a, LNPs). The luminescence core ($NaGdF_4$:Yb,Er,Ce) has a *β*-$NaGdF_4$ crystalline structure co-doped with 78% Yb^{3+}, 2% Er^{3+}, and 5% Ce^{3+}, and has a diameter of 37.1 ± 2.46 nm (Fig. S1a, b,† Core). The NIR absorption shell contained 50% of Yb^{3+} for the absorption of 980 nm excitation light and 50% of Nd^{3+} for the absorption of 808 nm excitation light. The obtained $NaGdF_4$:Yb,Er,Ce@$NaYbF_4$:Nd showed a core–shell structure with the particle diameter increased to 67.1 ± 3.01 nm (Fig. S1a, b,† CS1). The continuous growth of the inert shell $NaGdF_4$ eliminated the surface-related quenching of luminescence, resulting in LNPs with a particle diameter of 77.7 ± 3.43 nm (Fig. 1a and Fig. S1a, b,† LNPs). X-ray diffraction (XRD) patterns of LNPs showed a highly crystalline hexagonal phase consistent with the β-$NaGdF_4$ standard pattern (JCPDS: 27-0699) (Fig. S1c†). The elemental mapping and electron imaging results of the obtained LNPs further confirm the core–shell structure with distinct compositional boundaries. The F element shows a uniform distribution throughout the nanoparticle, while the Yb element also displays continuous distribution in the luminescence core and NIR absorption shell. The Gd element is significantly enriched in the outermost inert shell, while the Nd element and Ce/Er elements are concentrated in the middle NIR absorption shell and luminescence core, respectively (Fig. 1a). Multiplexed downconversion and upconversion luminescence of LNPs were achieved *via* 980/808 nm excitations. The 980 nm excitation light energy was absorbed by the sensitizer Yb^{3+} and migrated over the

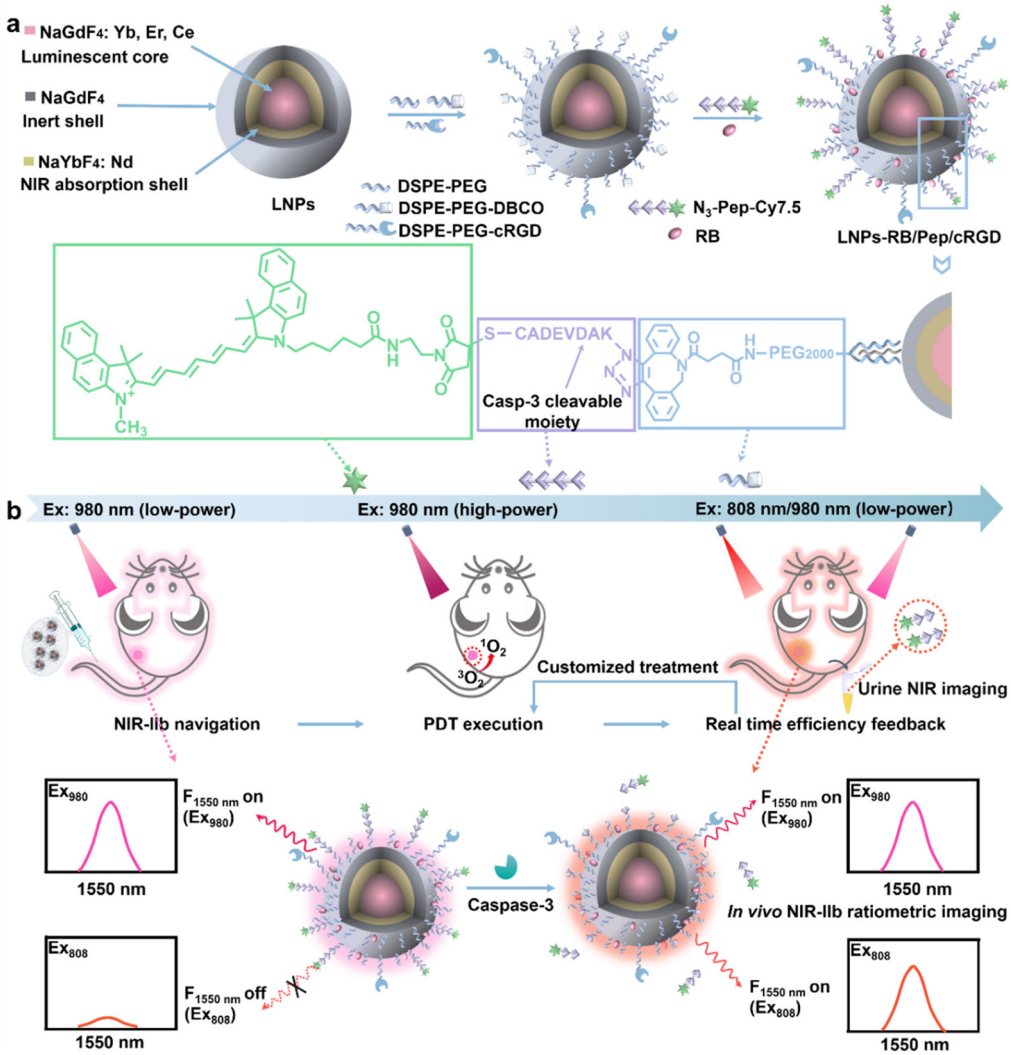

Scheme 1 Schematic illustration of programming LNP luminescence for customized cancer treatment. (a) Construction and synthesis of LNPs-RB/Pep/cRGD, and (b) its application in NIR-IIb imaging-guided PDT with real-time efficiency feedback *via in vivo* ratiometric NIR-IIb fluorescence imaging and urinalysis.

Yb^{3+} sublattice through interionic cross-relaxation, finally being entrapped by the activator Er^{3+} in the luminescence core and excited to the intermediate $^4I_{11/2}$ level. The rapid nonradiative decay from Er^{3+} $^4I_{11/2}$ to $^4I_{13/2}$, followed by subsequent radiative relaxation to the $^4I_{15/2}$ state, produced downconversion luminescence at 1550 nm.[24] The long-lived intermediate $^4I_{11/2}$ state of Er^{3+} was excited further to higher energy states, producing upconversion luminescence at 542 nm ($^4S_{3/2} \rightarrow {}^4I_{15/2}$) and 650 nm ($^4F_{9/2} \rightarrow {}^4I_{15/2}$) (Fig. 1b). Ce^{3+} was doped into the luminescence core to promote nonradiative relaxation of Er^{3+} $^4I_{11/2} \rightarrow {}^4I_{13/2}$, enhancing downconversion luminance at 1550 nm, while suppressing its upconversion emissions at 542 nm and 650 nm.[40] The doping percentage of Ce^{3+} was optimized as 5% to achieve maximum enhancement for downconversion luminescence at 1550 nm with the least concession of upconversion luminescence at 542 nm under 980 nm excitation (Fig. S2a and b†), qualifying LNPs for phototherapy with real-time *in vivo* imaging for therapeutic efficiency feedback. The 808 nm excitation light energy was absorbed by the sensitizer Nd^{3+} in the middle NIR absorption shell, $NaYbF_4$:Nd, to reach the excited state of $^4F_{5/2}$. Part of the energy was transferred by Yb^{3+} as an energy bridge to excite Er^{3+}, emitting NIR-IIb luminescence at 1550 nm (Fig. S2c†). The obtained LNPs had oleic acid (OA) as a surface ligand, therefore, they were modified with amphiphilic polymer, DSPE-PEG/DSPE-PEG-DBCO, *via* hydrophobic–hydrophobic interaction between OA and DSPE to enable them to transfer into aqueous solutions. The as-obtained LNPs-PEG-DBCO showed good dispersion in aqueous solution (Fig. S3†), exhibiting intensive upconversion luminescence at 542/650 nm and NIR-IIb luminescence at 1550 nm under 980 nm excitation (Fig. 1c, LNPs-PEG-DBCO) and 1550 nm luminance under 808 nm excitation (Fig. 1d, LNPs-PEG-DBCO). The absolute quantum yields of upconversion and downconversion emissions of LNPs

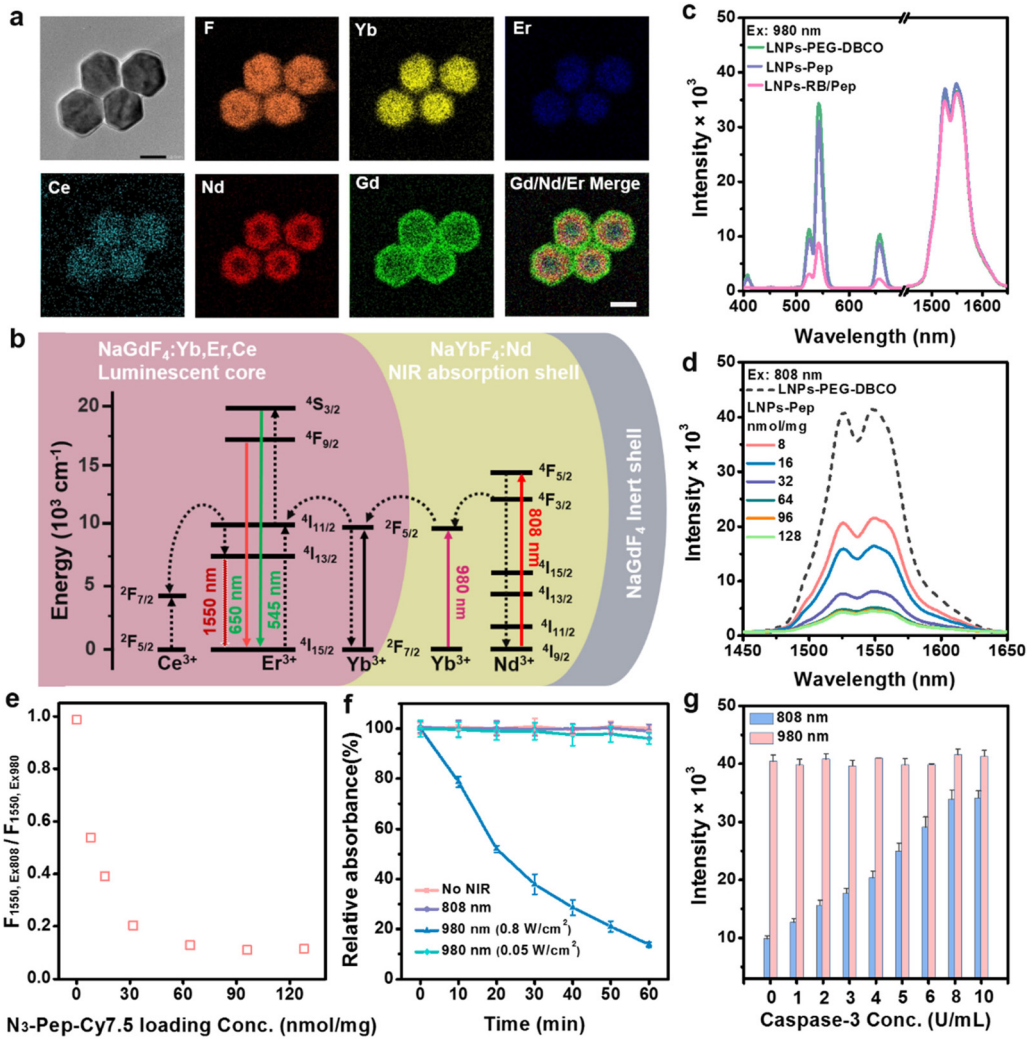

Fig. 1 Synthesis of LNPs-RB/Pep and characterization of ROS generation and caspase-3 response. (a) Element mapping and (b) energy-transfer mechanisms of LNPs $NaGdF_4$:Yb,Er,Ce@$NaYbF_4$:Nd@$NaGdF_4$. Scale bars: 50 nm. (c) Upconversion emission and downconversion luminance spectra of LNPs-PEG-DBCO, LNPs-Pep, and LNPs-RB/Pep under 980 nm excitation, (d) downconversion luminance spectra of LNPs-PEG-DBCO and LNPs-Pep (with N_3-Pep-Cy7.5 loading concentrations of 8–128 nmol mg^{-1}) under 808 nm excitation and (e) corresponding linear relationship for NIR-IIb luminance ratio ($F_{1550,\ Ex808}/F_{1550,\ Ex980}$) over N_3-Pep-Cy7.5 loading concentration, (f) time-dependent relative absorption percentages of DPBF at 410 nm for LNPs-RB/Pep under different times of high power 980 nm (0.8 W cm^{-2}), 808 nm, and low power 980 nm (0.05 W cm^{-2}) excitation. (g) Luminance intensity at 1550 nm for LNPs-RB/Pep in response to different concentrations of caspase-3 (0–10 U mL^{-1}) at 37 °C for 3 h under 808 nm and 980 nm excitations. The error bars in (e) to (g) indicated means ± S.D. (n = 3).

under 980 nm and 808 nm laser excitations were calculated with a fluorescence spectrometer incorporating an integrating sphere, which yielded 2.42% and 14.02% for NIR-II emission (1450–1650 nm) under 980 nm and 808 nm excitations, respectively, and 2.73% for visible emission (500–570 nm) under 980 nm (Fig. S4†).

To endow the above obtained LNPs-PEG-DBCO with caspase-3 imaging capability, the caspase-3 substrate peptide KADVEDAC was functionalized with azide at the lysine terminus and Cy7.5 at the cysteine terminus (N_3-Pep-Cy7.5) and conjugated to LNPs-PEG-DBCO *via* a click reaction to yield LNPs-Pep. N_3-Pep-Cy7.5 was produced through a maleimide reaction between cysteine and Cy7.5-Mal, confirmed *via* HPLC (Fig. S5a†) and MALDI-TOF mass (Fig. S5b†) analysis. LNPs-PEG-DBCO showed a hydrodynamic diameter of 107.3 ± 8.6 nm with a zeta potential of −5.05 ± 0.34 mV due to the PEG polymer coating (Fig. S6,† (1) LNPs-PEG-DBCO). The conjugation of N_3-Pep-Cy7.5 increased the hydrodynamic diameter to 132.09 ± 10.6 nm with a zeta potential of −9.65 ± 0.19 mV due to the negative charge of N_3-Pep-Cy7.5 (Fig. S6,† (2) LNPs-Pep). The obtained LNPs-Pep also demonstrated a Cy7.5 absorbance at 790 nm (Fig. S7a,† LNPs-Pep). Due to the larger molar extinction coefficient of Cy7.5 dye compared to the LNPs sensitizer Nd^{3+} at ~790 nm (Fig. S7a,† Cy7.5, Nd^{3+}), it served as an efficient photon-filter for 808 nm excitation energy based on absorption competition-induced emission (ACIE) and caused

notable loading-dependent suppression of LNPs NIR-IIb emission at 1550 nm under 808 nm excitation (Fig. 1d). Cy7.5 barely showed absorbance at 980 nm (Fig. S7a,† Cy7.5), thus did not affect NIR-IIb downconversion emission of LNPs at 1550 nm or upconversion emission of LNPs at 542 nm under 980 nm laser excitation (Fig. 1c, LNPs-Pep and Fig. S7b†). With the increasing amount of N_3-Pep-Cy7.5 modified on the LNPs surface, the ratio of 1550 nm emission under 808 nm excitation over 980 nm excitation ($F_{1550,\ Ex808}/F_{1550,\ Ex980}$) displayed exponential decay, saturating at ~87% with an N_3-Pep-Cy7.5 loading amount of 64 nmol mg^{-1} (Fig. 1e). The photosensitizer rose bengal (RB) was also loaded onto the obtained LNPs-PEG-DBCO *via* hydrophobic–hydrophobic interaction with DSPE, which qualified the obtained LNPs-RB/Pep for PDT with real-time efficiency feedback *via* caspase-3 imaging. Subsequent RB loading resulted in a hydrodynamic diameter of 143.08 ± 13.7 nm with a zeta potential of −11.3 ± 0.2 mV (Fig. S6,† (3) LNPs-RB/Pep). RB has characteristic absorption in the 480–600 nm region, which overlaps well with LNP upconversion emission at 542 nm under 980 nm excitation (Fig. S7c†). The obtained LNPs-RB/Pep showed a characteristic absorption peak of RB at 568 nm (Fig. S7a,† LNPs-RB/Pep) with a decrease in upconversion emission peak intensity at 542 nm under 980 nm excitation (Fig. 1c, LNPs-RB/Pep). The loading of RBs onto LNPs-Pep did not affect its downconversion emission peat at 1550 nm under 980 nm excitation (Fig. 1c, LNPs-RB/Pep).

The capability of the as-obtained LNPs-RB/Pep to generate ROS under high-power 980 nm irradiation (0.8 W cm^{-2}) was assessed using the ROS-sensitive probe, 1,3-diphenylisobenzofuran (DPBF).[41] The characteristic absorbance peak of DPBF at 412 nm obviously decreased by 86.3% within 60 min, indicating rapid ROS consumption (Fig. S8a†). 808 nm irradiation and low power 980 nm irradiation (0.05 W cm^{-2}) did not generate ROS. Therefore, DPBF characteristic absorption peaks remained at the same intensities (Fig. S8b and c†). *In vitro* ROS generation was further assessed using the fluorescent probe, DCFH-DA. The probe was first hydrolyzed to DCFH in PBS buffer and incubated in the dark for 20 min. Subsequently, it was incubated with LNPs-RB/Pep and exposed to varying durations of 980 nm irradiation (0.8 W cm^{-2}). The fluorescence intensity of DCFH-DA increased gradually with irradiation time, demonstrating a sensitive response to ROS (Fig. S8d–g†). These results indicated effective manipulation of photodynamic therapy (PDT) with different wavelengths and powers of irradiation lights (Fig. 1f).

Caspase-3 protease cleaved its substrate peptide KADVEDAC, detaching the Cy7.5-containing fragment (Cy7.5-CADEVD) from the LNPs surface, which terminated the ACIE process and recovered the 1550 nm downconversion emission under 808 nm irradiation (Fig. S9a†), while the 1550 nm downconversion emission under 980 nm remained unchanged (Fig. S9b†). The 1550 nm emission intensity ratio under 808 nm excitation and 980 nm excitation ($F_{1550,\ Ex808}/F_{1550,\ Ex980}$) was calculated, showing a significant increase, according to caspase 3 reaction time and saturating at 3 h (Fig. S9c†). This result indicated a fast response of LNPs-RB/Pep to caspase-3, confirming its applicability for real-time therapeutic efficiency feedback. Different concentrations of caspase-3 from 0 to 10 U mL^{-1} were also used to treat LNPs-RB/Pep, resulting in a concentration-dependent increase of 1550 nm emission under 808 nm irradiation, with the 1550 nm emission intensity under 980 nm irradiation remaining unchanged (Fig. 1g and S10a, b†). The plot of $F_{1550,\ Ex808}/F_{1550,\ Ex980}$ *versus* caspase-3 concentration exhibited a detectable range with a linear correlation up to 8 U mL^{-1}, providing a detection limit of 0.111 U mL^{-1} (Fig. S10c†). The supernatant was also collected after enzymatic cleavage to measure Cy7.5 characteristic emission peak at 820 nm, which showed a gradual increase corresponding to caspase-3 concentration (Fig. S11†). The strong emission intensity of Cy7.5 in the NIR region indicated the capability of urinalysis-cleaved Cy7.5-CADEVD for caspase-3 qualification. LNPs-RB/Pep also demonstrated high selectivity for caspase-3 (Casp-3) protease over other proteases and ions under physiological conditions, showing a high ratio value of $F_{1550,\ Ex808}/F_{1550,\ Ex980}$ for caspase-3 (Fig. S12†).

2.2. Synthesis of LNPs-RB/Pep/cRGD and verification of its therapeutic efficiency feedback capability at the cellular level

LNPs were also functionalized with a cyclic peptide amphiphilic polymer (DSPE-PEG-cRGD) that targets the $\alpha_v\beta_3$ integrin receptor to facilitate active delivery.[42] Modification of DSPE-PEG-cRGD barely affected the properties of LNPs-RB/Pep, and the as-obtained LNPs-RB/Pep/cRGD showed a similar morphology to LNPs-PEG-DBCO (Fig. S13a†) with DLS of 156.37 ± 16.9 nm and zeta potential of −12.5 ± 0.31 mV (Fig. S6,† (4) LNPs-RB/Pep/cRGD). LNPs-RB/Pep/cRGD demonstrated stable downconversion NIR-IIb emission and upconversion emission intensities under 980 nm excitation (Fig. S14a†) and downconversion NIR-IIb emission under 808 nm excitation (Fig. S14b†) in saline and serum. Both downconversion and upconversion luminescence demonstrated stable intensities upon 10 min of 808 nm and 980 nm low power (0.05 W cm^{-2}) irradiations (Fig. S14c†), indicating good photostability of LNPs-RB/Pep/cRGD. LNPs-RB/Pep/cRGD did not aggregate in saline or DMEM with FBS, showing little increase in DLS during 7 days of incubation (Fig. S14d†).

Human hepatocellular carcinoma HCCLM3 cells (purchased from Keygen Biotech (Nanjing, China)) which overexpress the $\alpha_v\beta_3$ integrin receptor on their cell membrane, were chosen as the sample cells to incubate with LNPs-RB/Pep/cRGD, resulting in obvious intracellular RB luminescence. Conversely, HCCLM3 cells incubated with LNPs-RB/Pep demonstrated little intracellular RB luminescence (Fig. S13b†). This result indicates the effective and specific endocytosis of LNPs-RB/Pep/cRGD by cancer cells. Intracellular ROS generation was measured with 2′,7′-dichlorodihy-drofluorescein diacetate (DCFH-DA), which emits at 517 nm under 492 nm excitation due to ROS oxidation.[43] Treatment of HCCLM3 cells with LNPs-RB/Pep/cRGD followed by 980 nm (0.8 W cm^{-2}) irradiation resulted in a remarkable intracellular DCFH-DA fluorescence, indicating high efficiency of ROS generation

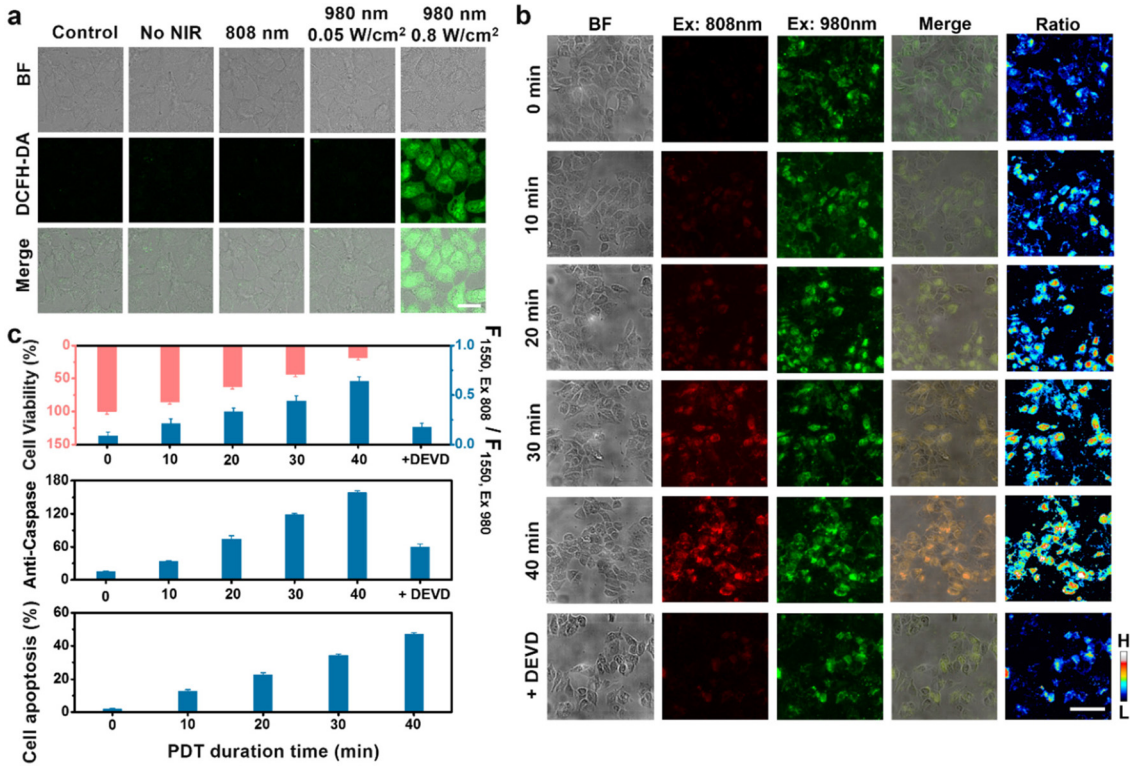

Fig. 2 Verification of LNPs-RB/Pep/cRGD PDT efficiency and capability of therapeutic effect self-evaluation. (a) Confocal microscopic images of untreated HCCLM3 cells (control), LNPs-RB/Pep/cRGD-incubated HCCLM3 cells (No NIR) for 4 h, and LNPs-RB/Pep/cRGD-incubated HCCLM3 cells under 980 nm (0.8 W cm^{-2} and 0.05 W cm^{-2}, respectively), 808 nm irradiation. All cells were stained with DCFH-DA. Scale bar: 25 μm. (b) Representative NIR-IIb fluorescence and ratio images of LNPs-RB/Pep/cRGD pretreated HCCLM3 cells for 4 h and then exposed to different PDT duration periods (0–40 min), and HCCLM3 cells pretreated with LNPs-RB/Pep/cRGD and extra peptide CADEVDAK before 40 min PDT (+DEVD). Images were taken at 12 h after PDT, scale bar: 100 μm. (c) Corresponding ratiometric NIR-IIb fluorescence intensity at 808 nm excitation over 980 nm excitation ($F_{1550,\ Ex808}/F_{1550,\ Ex980}$), intracellular caspase-3 expression (anti-Caspase), cell apoptosis, and cell viability. The error bars indicate mean ± S.D. (n = 3).

(Fig. 2a, 980 nm, 0.8 W cm^{-2}). Conversely, DCFH-DA fluorescence was barely observed in control groups of LNPs-RB/Pep/cRGD-treated HCCLM3 cells under 808 nm irradiation and low power 980 nm (0.05 W cm^{-2}) irradiation (Fig. 2a, 808 nm, 980 nm, 0.05 W cm^{-2}). These results indicate good precision in executing PDT by manipulating NIR irradiation. LNPs-RB/Pep/cRGD-treated HCCLM3 cells showed over 99% viability in the absence of NIR irradiation, and under both 808 nm and low power 980 nm irradiation (0.05 W cm^{-2}), indicating good biocompatibility of LNPs-RB/Pep/cRGD (Fig. S15a,† No NIR, 808 nm, 980 nm (0.05 W cm^{-2})). Under high power 980 nm irradiation (0.8 W cm^{-2}), LNPs-RB/Pep/cRGD demonstrated concentration-dependent anticancer activities against HCCLM3 cells, with cell viability decreasing to 13.7% for HCCLM3 cells treated with 200 μg mL^{-1} LNPs-RB/Pep/c-RGD (Fig. S15a,† 980 nm (0.8 W cm^{-2})). Flow cytometry assays using Annexin V-fluorescein isothiocyanate FITC/PI apoptotic kit also demonstrated increased apoptotic effects, corresponding to LNPs-RB/Pep/cRGD concentration under high power 980 nm irradiation (0.8 W cm^{-2}), with the apoptosis rate reaching 75.2% for 200 μg mL^{-1} LNPs-RB/Pep/cRGD-treated HCCLM3 cells under high power 980 nm irradiation (0.8 W cm^{-2}) (Fig. S15b and c†).

Cell apoptosis is featured by intracellular caspase-3 generation, which cleaved the Cy7.5-containing substrate peptide (Cy7.5-CADEVDAK) modified on the LNPs-RB/Pep/cRGD surface. The release of the Cy7.5-containing fragment (Cy7.5-CADEVD) resulted in an apparent recovery of 1550 nm NIR-IIb fluorescence under 808 nm excitation (Fig. S16a, b,† Ex: 808 nm). As Cy7.5 has little absorption at 980 nm, the cleavage of Cy7.5-containing peptide did not affect the 1550 nm NIR-IIb luminescence of LNPs-RB/Pep/c-RGD under 980 nm excitation (Fig. S16a, b,† Ex: 980 nm). Intracellular caspase-3 generation in HCCLM3 cells was monitored in real-time after high-power 980 nm irradiation (0.8 W cm^{-2}), and the ratio of fluorescence intensity in the 1450–1700 nm region at 808 nm irradiation over low power 980 nm irradiation (0.05 W cm^{-2}) was taken. A distinguishable ratio image was observed as early as 4 h after PDT, demonstrating a time-dependent intensity increase that reached its maximum value at 12 h after PDT (Fig. S16a,† Ratio, c).

To verify the capability of LNPs-RB/Pep/cRGD as a multiplex platform for PDT with self-evaluation of therapeutic efficiency, the cells were exposed to 980 nm irradiation (0.8 W cm^{-2}) for different time periods (0, 10, 20, 30, 40 min, with 5 min break

between each 10 min exposure). NIR-IIb images under 808 nm irradiation over 980 nm irradiation were collected at 12 h post-PDT to monitor caspase-3 generation. The NIR-IIb imaging under 808 nm irradiation showed a continued increase with PDT duration time, while NIR-IIb imaging under 980 nm irradiation maintained a similar intensity (Fig. 2b, Ex: 808 nm, Ex: 980 nm and Fig. S17a,† 0–40 min). The NIR-IIb fluorescence ratio ($F_{1550,\ Ex808}/F_{1550,\ Ex980}$) increased according to the irradiation period, indicating enhanced caspase-3 generation with longer PDT duration time (Fig. 2b, Ratio and Fig. 2c, $F_{1550,\ Ex808}/F_{1550,\ Ex980}$, 0–40 min). To confirm that the ratio image intensity increase was due to caspase-3 activation, control experiments were set by incubating LNPs-RB/Pep/cRGD-treated HCCLM3 cells with free external substrate peptide (CADEVDAK), which acted as a competitive reactant for Cy7.5-CADVED that was modified on LNPs-RB/Pep/cRGD. Free CADEVDAK showed reaction superiority to caspase-3, which impaired the reaction efficiency of caspase-3 with LNPs-RB/Pep/cRGD. This resulted in significant suppression of both LNPs-RB/Pep/cRGD NIR-IIb fluorescence recovery under 808 nm excitation and NIR-IIb fluorescence ratio value ($F_{1550,\ Ex808}/F_{1550,\ Ex980}$) (Fig. S17a† and Fig. 2b, Ratio, +DEVD, and Fig. 2c, $F_{1550,\ Ex808}/F_{1550,\ Ex980}$, +DEVD). This reaction ensured that NIR-IIb fluorescence recovery observed for PDT was due to a specific caspase-3 reaction, instead of nonspecific Cy7.5-CADVED falling from the LNPs' surface. The intracellular expression of activated caspase-3 followed PDT was also confirmed by immunofluorescence, which demonstrated a similar tendency of increased intracellular Cy3 fluorescence from a Cy3-labelled caspase-3 antibody (anti-Caspase), corresponding to PDT irradiation periods (Fig. S17b† and 2c, anti-Caspase, 0–40 min). Active caspase-3 translocates from the cytoplasm into the nucleus of apoptotic cells, either with some substrate proteins[44] or simply diffusing into nuclei after the disruption of the nuclear-cytoplasmic barrier.[45] Therefore, anti-Caspase staining was also observed in the nucleus. The control group treated with the extra substrate peptide, CADEVDAK, showed a significant decrease in the intensity of intracellular Cy3 fluorescence, attributed to the depletion of active caspase-3 in apoptotic cells by CADEVDAK (Fig. S17b† and 2c, anti-Caspase, +DEVD). These results confirm the accuracy of the LNPs-RB/Pep/cRGD ratio image for reporting intracellular caspase-3 expression levels. Cell apoptosis also demonstrated a similar trend, increasing with PDT duration (Fig. S17c† and 2c, cell apoptosis). Cell viability was also evaluated for LNPs-RB/Pep/cRGD-incubated HCCLM3 cells, which decreased according to PDT duration (Fig. 2c, cell viability). A strong correlation was observed for the NIR-IIb ratio image ($F_{1550,\ Ex\ 808}/F_{1550,\ Ex980}$) of LNPs-RB/Pep/cRGD, intracellular caspase-3 expression, cell apoptosis percentage, and cell viability percentage, confirming the capability of LNPs-RB/Pep/cRGD as a multiplex PDT platform with self-evaluation of therapeutic efficiency.

2.3. Programming NIR irradiation for NIR-IIb imaging-guided PDT and real-time efficiency feedback

Balb/c nude mice (4–5 weeks, female) were chosen for establishing the tumor model due to their high success rate in tumour formation and reproducibility. All animal procedures were performed in accordance with the Guidelines for Care and Use of Laboratory Animals at Nanjing University and approved by the Animal Ethics Committee of Nanjing University with an approval number of IACUC-2303006. Each mouse was subcutaneously injected with 1×10^7 HCCLM3 cells in the right leg to generate a subcutaneous tumor animal modal. The HCCLM3 tumor-bearing mice were chosen as the *in vivo* model to verify the capability of LNPs-RB/Pep/cRGD as a multiplex platform for NIR-IIb imaging-guided PDT with real-time efficiency feedback. After intravenous injection of LNPs-RB/Pep/cRGD, its systematic circulation was monitored by NIR-IIb imaging under low power 980 nm irradiation (0.05 W cm^{-2}), indicating the optimal time point for LNPs-RB/Pep/cRGD accumulation at the tumor site to perform phototherapy (Fig. 3a, NIR-IIb imaging navigation). The mice's whole-body vessels were clearly visualized within 4 h post-injection, indicating good systematic circulation of LNPs-RB/Pep/cRGD (Fig. S18,† Ex: 980 nm). The tumor position began to show NIR-IIb fluorescence at 1 h post-injection, which increased with time, reaching maximum intensity at 9 h post-injection, indicating efficient accumulation of LNPs-RB/Pep/cRGD at the tumor position Therefore, 9 h post-injection was chosen as the time point to perform PDT. Due to metabolic clearance of LNPs-RB/Pep/cRGD, NIR-IIb fluorescence under low power 980 nm irradiation decreased after 9 h post-injection (Fig. 3b, $F_{1550,\ Ex980}$). In comparison, LNPs-RB/Pep/cRGD showed little NIR-IIb fluorescence under 808 nm irradiation (Fig. S18,† Ex: 808 nm and Fig. 3b, $F_{1550,\ Ex808}$), indicating little nonspecific activation of NIR-IIb fluorescence and few false positive imaging signals from caspase-3 during the systematic circulation process.

PDT was performed using high-power 980 nm laser irradiation (0.8 W cm^{-2}) for 40 min (with 5 min breaks between each 10 min exposure) at tumor lesions (Fig. 3a, PDT). The thermal images of tumor-bearing mice showed that the local temperature at the tumor position remained at 36.9 °C during the test period of 10 min under 980 nm irradiation (0.8 W cm^{-2}). Following 10 min of 980 nm (0.8 W cm^{-2}) NIR irradiation, there was a 5 min break, during which the local temperature rapidly decreased to normal levels (Fig. S19†). These results indicate that there was no thermal damage to tissue with the above irradiation conditions. PDT generated caspase-3 to cleave Cy7.5-containing peptide fragment (Cy7.5-CADVED) off from LNPs-RB/Pep/cRGD, consequently recovering LNPs-RB/Pep/cRGD NIR-IIb fluorescence under 808 nm irradiation. Therefore, the intensity of $F_{1550,\ Ex808}$ continued to increase and reached a peak value at 12 h post-PDT, followed by a corresponding decrease in intensity due to the metabolism of LNPs-RB/Pep/cRGD (Fig. 3c, Ex: 808 nm and Fig. 3d, $F_{1550,\ Ex808}$). The production of caspase-3 did not affect LNPs-RB/Pep/cRGD NIR-IIb fluorescence under lower power 980 nm irradiation (0.05 W cm^{-2}), and $F_{1550,\ Ex980}$ demonstrated a time-corresponding intensity decrease due to the metabolism of LNPs-RB/Pep/cRGD (Fig. 3c, Ex: 980 nm and Fig. 3d, $F_{1550,\ Ex980}$). The NIR-IIb ratiometric imaging under 808 nm compared to 980 nm was collected as feedback

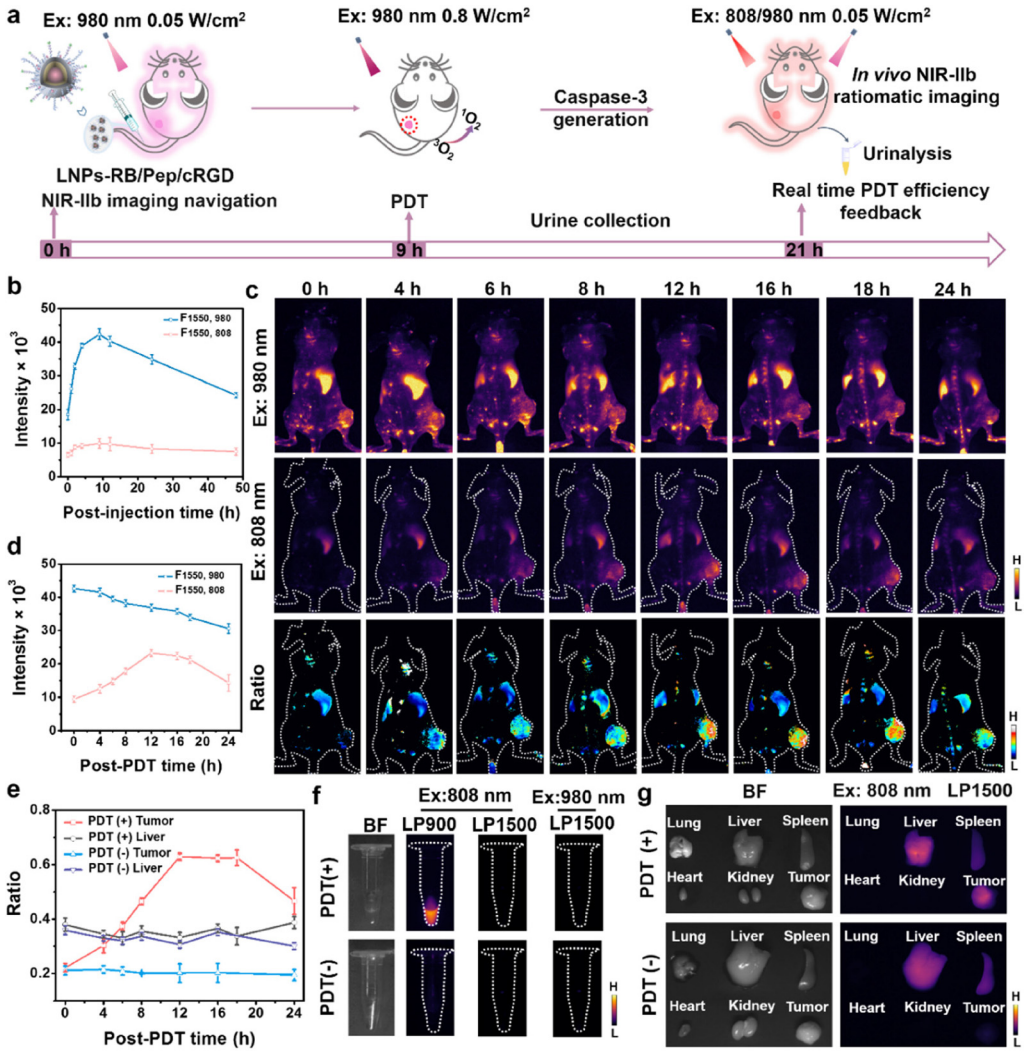

Fig. 3 Application of LNPs-RB/Pep/cRGD in NIR-IIb imaging-guided PDT and real-time efficiency feedback. (a) Schematic illustration of the therapeutic process, including NIR-IIb imaging-guided PDT and real-time efficiency feedback *via in vivo* ratiometric NIR-IIb fluorescence imaging and *in vitro* urinalysis. (b) NIR-IIb fluorescence intensity in tumor lesions after intravenous injection of LNPs-RB/Pep/cRGD under 980 and 808 nm excitation with LP1500 long-pass filter. (c) *In vivo* NIR-IIb fluorescence under low power 980 nm irradiation (0.05 W cm^{-2})/808 nm irradiation and ratio images at different times post-PDT and (d) time corresponding $F_{1550,\ Ex808}$ and $F_{1550,\ Ex980}$ intensities. (e) Ratiometric NIR-IIb fluorescence value ($F_{1550,\ Ex808}/F_{1550,\ Ex980}$) in tumor and liver for the presence (PDT (+)) and absence of PDT (PDT (–)). (f) Fluorescence images of mice urine collection over 12 h post-PDT under 980 nm and 808 nm excitation with LP900 and LP1500 long-pass filter. (g) Bright-field and the NIR-IIb fluorescence images of main organs (heart, liver, lung, spleen, and kidney) 12 h post-PDT under 808 nm excitation with LP1500 long-pass filter in the presence (PDT (+)) and absence of PDT (PDT (–)). The error bars in (c) and (d) indicate means ± S.D. (n = 3). PDT was performed with 5 min breaks between each 10 min exposure.

for PDT efficiency (Fig. 3a, *in vivo* NIR-IIb ratiometric imaging). Meanwhile, Cy7.5-CADVED was rapidly cleared by the kidneys, enabling the urinalysis of Cy7.5 fluorescence as an extra evaluation approach for PDT efficiency (Fig. 3a, Urinalysis). NIR-IIb ratiometric imaging $F_{1550,\ Ex808}/F_{1550,\ Ex980}$ in the tumor was conducted to eliminate the interference of nanoprobe metabolism on imaging accuracy, which gradually increased over time and saturated during the period of 12–18 h post-PDT. During the later measurement period, after 18 h post-PDT, both $F_{1550,\ Ex808}$ and $F_{1550,\ Ex980}$ substantially decreased, resulting in very low signal intensity at the tumor position, especially for $F_{1550,\ Ex808}$ (Fig. 3d, $F_{1550,\ Ex808}$), which correspondingly caused a decrease in the ratio value $F_{1550,\ Ex808}/F_{1550,\ Ex980}$ (Fig. 3c, Ratio and Fig. 3e, PDT (+) Tumor). Therefore, 12 h post-PDT was chosen as the time point for NIR-IIb *in vivo* imaging to report the therapeutic effect. A no-treatment control was set by intravenously injecting LNPs-RB/Pep/cRGD into HCCLM3 tumor-bearing mice in the absence of high-power 980 nm laser irradiation (0.8 W cm^{-2}), which did not show a distinguishable NIR-IIb ratio image due to the absence of caspase-3 generation (Fig. S20† and Fig. 3e, PDT (–) Tumor). As most of the administrated nanoprobes accumulated in the liver, background NIR-IIb fluorescence was also observed in the liver for both the PDT execution group and the

no-treatment control group (Fig. 3c, Ratio and Fig. S20,† Ratio) from "unactivated" LNPs-RB/Pep/cRGD due to its fluorescence being incompletely quenched under 808 nm excitation (Fig. 1d, 64 nmol mg^{-1}). The ratio image $F_{1550,\ Ex808}/F_{1550,\ Ex980}$ from the tumor position for the PDT execution group was significantly higher than that of background ratio image $F_{1550,\ Ex808}/F_{1550,\ Ex980}$ from the liver position, confirming the successful generation of PDT and corresponding cell apoptosis (Fig. 3e, PDT(+) Tumor, PDT(+) Liver).

The urine of mice was also collected over 12 h after PDT for fluorescence measurement to further verify caspase-3 generation, which demonstrated a Cy7.5 characteristic absorption peak at 790 nm and a wide emission region of 800–1000 nm due to the metabolism of cleaved Cy7.5-CADVED into systemic circulation (Fig. S21†). The mice urine collection showed strong fluorescence intensity in the presence of high power 980 nm irradiation (PDT (+)) and little fluorescence in the absence of high power 980 nm irradiation (PDT (−)) *via* a NIR-II *in vivo* imaging system with LP900 long-pass filter, further confirming the successful operation of PDT and corresponding generation of caspase-3 (Fig. 3f, Ex: 808 nm, LP 900). Considering the over 100 nm size of LNPs-RB/Pep/cRGD, they took the biliary excretion pathway[46,47] and were hardly metabolized into the urine, thus showing little fluorescence signal with LP1500 long-pass filter either under 980 nm or 808 nm excitation (Fig. 3f, Ex: 808 nm, LP 1500; Ex: 980 nm, LP 1550). The *ex vivo* fluorescence images of major organs and tumors were also collected from mice at 12 h post-PDT treatment, showing obvious NIR-IIb fluorescence signal over 1500 nm in tumor under 808 nm irradiation (Fig. 3g, PDT(+), Tumor). Conversely, the control group in the absence of PDT barely showed NIR-IIb fluorescence under 808 nm irradiation from the tumor due to the lack of caspase-3 generation (Fig. 3g, PDT (−), Tumor). This result confirmed the efficient operation of PDT. The continued accumulation of unactivated LNPs-RB/Pep/cRGDs resulted in background fluorescence, so the liver also displayed NIR-IIb fluorescence signal (Fig. 3g, PDT(+), PDT(−) Liver). Urine fluorescence measurement and *ex vivo* fluorescence imaging further confirmed the capability of LNPs-RB/Pep/cRGD for self-evaluation of *in situ* PDT efficiency.

2.4. Customized PDT with real-time efficiency feedback

To evaluate the accuracy of LNPs-RB/Pep/cRGD and corresponding *in vivo* NIR-IIb imaging/*in vitro* NIR urinalysis for real-time therapeutic efficiency evaluation, tumor-bearing mice were divided into four groups (n = 3), which were treated with different durations (0, 10, 20, 40 min) of PDT, respectively, *via* high power 980 nm NIR irradiations. The ratiometric NIR-IIb fluorescence images under 808 nm irradiation over low power 980 nm irradiation ($F_{1550,\ Ex808}/F_{1550,\ Ex980}$) were acquired 12 h post-PDT, and urine samples were collected over the same time period (Fig. 4a). Both NIR-IIb ratiometric fluorescence images (Fig. 4b) and urine NIR fluorescence (Fig. 4c) increased according to the PDT duration. The ratiometric NIR-IIb fluorescence imaging ratio value gradually increased with PDT duration, reaching 4.01-fold and 2.03-fold for the 40 min PDT treatment group compared with the control group without PDT and the 10 min PDT treatment group, respectively (Fig. S22,† $F_{1550,\ Ex\ 808}/F_{1550,\ Ex980}$). Urine NIR fluorescence for the 40 min PDT treatment group was 4.03-fold and 2.38-fold compared with the control group without PDT and the 10 min PDT treatment group, respectively (Fig. S22,† Urine intensity). The tumor sizes of mice in different treatment groups were measured at day 14 to confirm the therapeutic efficiency, compared with the treatment control group that was treated with saline. The LNPs-RB/Pep/cRGD injected group without PDT showed barely any difference in the tumor size compared with the saline-treated group, while the PDT treatment groups (10 min, 20 min, and 40 min) showed tumor growth inhibition (Fig. S23,† Saline, 0 min, 10 min, 20 min, 40 min PDT), with size decreases of 37.4%, 64.1%, and 83.1%, respectively, compared with the saline-treated group (Fig. 4d, saline, 10 min, 20 min, 40 min PDT). The correlation between tumor size at 14 days post-treatment and caspase-3 activation measured by real-time fluorescence change at 12 h post-PDT was further investigated. The NIR-IIb fluorescence ratiometric values, urine NIR fluorescence intensity, and mice tumor volume all demonstrated negative correlations with PDT duration. The variations in the value of ratiometric NIR-IIb fluorescence (Fig. 4e) and urine NIR fluorescence intensity (Fig. 4f) were plotted against tumor volume for different treatment groups, and their Pearson's correlation coefficients were analyzed as −0.9586 (Fig. 4e) and −0.9714 (Fig. 4f), respectively, confirming that therapeutic efficiency could be evaluated by *in vivo* NIR-II fluorescence and urine NIR fluorescence measurements. The results from hematoxylin–eosin (H&E) staining, terminal transferase UTP nick end labeling (TUNEL) immunofluorescence staining, and immunohistochemistry of active caspase-3 (Casp-3 I&H) also demonstrated a similar tendency of cell apoptosis corresponding to PDT duration periods (Fig. S24,† Saline and 0–40 min). These results confirmed the capability of caspase-3-activated ratiometric NIR-IIb fluorescence imaging and *in vitro* urinary analysis as early evaluation tools for therapeutic effects and guaranteed their application in personalized treatment.

Traditional therapeutic effect evaluation approaches, such as tumor size evaluation, usually require patients to complete an entire treatment regimen before being diagnosed as ineffective, which can delay treatment adjustment and impair treatment outcomes. Caspase-3 real-time imaging provided efficacy feedback as early as 12 h after PDT, which is about one week earlier than traditional evaluation methods, thereby contributing to timely treatment dosage adjustments for individual cases. To demonstrate the application of LNPs-RB/Pep/cRGD to customized therapy, HCCLM3 tumor-bearing mice were divided into three groups (n = 3): "Caspase-3 evaluation" group, "size evaluation" group, and "control group". PDT treatment was applied every other day and repeated seven times. The control group was treated with 40 min of PDT irradiation for the whole experiment, while the "caspase-3 evaluation" and "size evaluation" groups underwent customized therapy based on therapeutic effect evaluation. The "caspase-3 evalu-

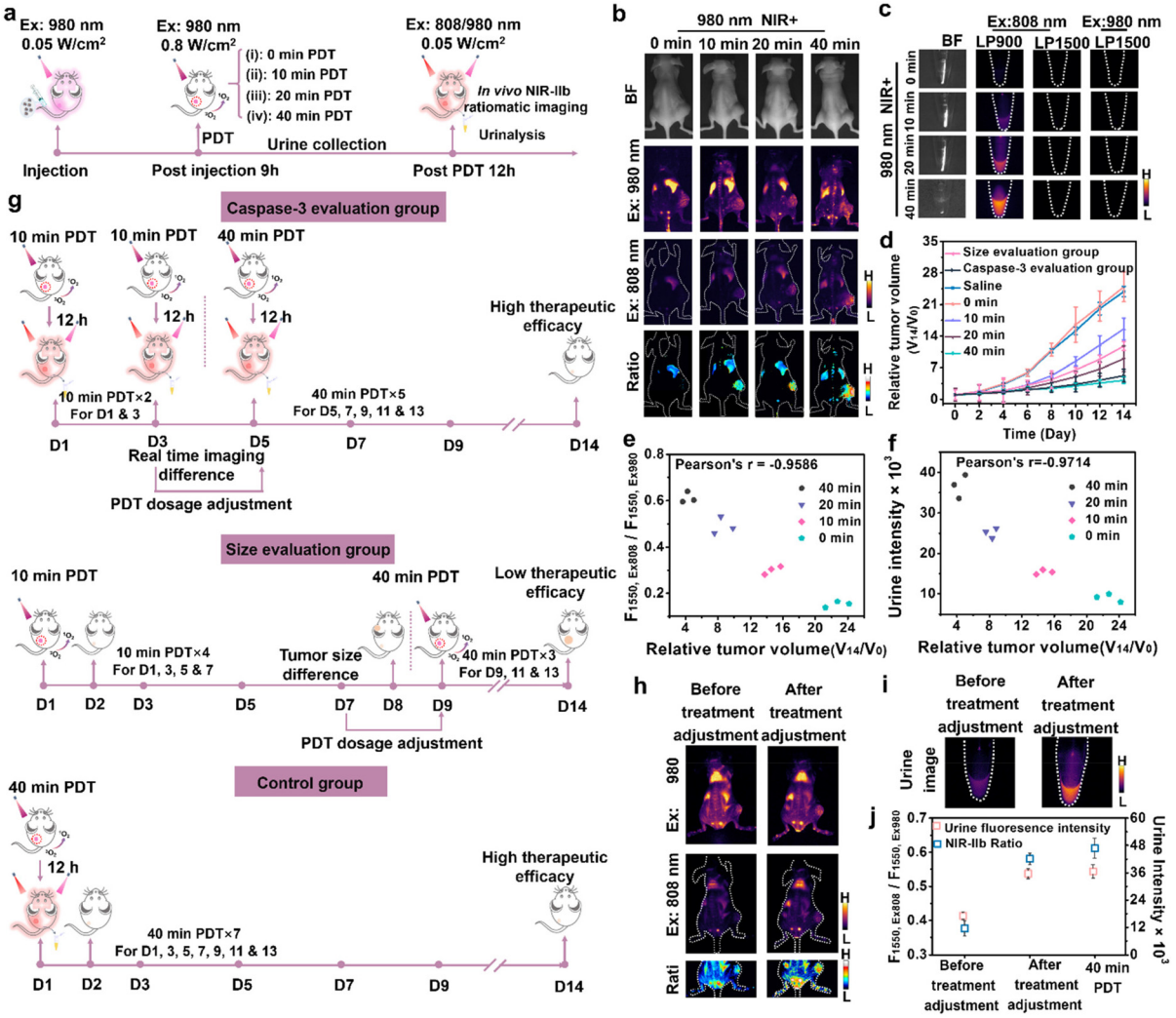

Fig. 4 Application of LNPs-RB/Pep/cRGD in customized PDT. (a) Schematic illustration of the therapeutic process, including NIR-IIb imaging-guided PDT and real-time efficiency feedback *via in vivo* ratiometric NIR-IIb fluorescence imaging and *in vitro* urinalysis for LNPs-RB/Pep/cRGD injected mice group under different PDT duration periods (0 min, 10 min, 20 min, and 40 min) and its corresponding. (b) *In vivo* NIR-IIb fluorescence image under low power 980 nm (0.05 W cm^{-2}) and 808 nm excitations with ratiometric image and (c) urine NIR fluorescence. (d) Time-dependent tumor growth for saline-injected mice group, LNPs-RB/Pep/cRGD injected mice group under different PDT durations (0 min, 10 min, 20 min, 40 min), and customized PDT groups with imaging evaluation and tumor size evaluation. Plotting of (e) ratiometric NIR-IIb fluorescence imaging value and (f) urine NIR fluorescence intensity at 12 h after PDT *versus* relative tumor volume at day 14. (g) Schematic illustration of customized PDT for caspase-3 evaluation group that operated with two times 10 min PDT and five times 40 min PDT, size evaluation group that operated with four sessions of 10 min PDT and three sessions of 40 min PDT and control group that operated with seven sessions of 40 min PDT. (h) *In vivo* NIR-IIb fluorescence imaging of LNPs-RB/Pep/cRGD injected mice under low power 980 (0.05 W cm^{-2}), 808 nm excitations, corresponding ratiometric images and (i) NIR fluorescence images of urine collection for "caspase-3 evaluation group". Images for "Before treatment adjustment" were taken after 2 sessions of 10 min PDT, and images for "After treatment adjustment" were taken after five sessions of 40 min PDT. (j) Ratiometric NIR-IIb fluorescence value ($F_{1550,\ Ex808}/F_{1550,\ Ex980}$) and urine NIR fluorescence intensity for before-treatment adjustment and after-treatment adjustment of imaging evaluation groups and 40 min PDT groups. The error bars in (d) and (i) indicate means ± S.D. (n = 3). PDT was performed with 5 min break after each 10 min exposure.

ation" group was treated with 10 min of 980 nm irradiation PDT, demonstrating *in vivo* NIR-IIb ratiometric imaging and *in vitro* urine fluorescence differences 12 h post-1st time PDT. The treatment of 10 min was repeated once, then adjusted to 40 min of PDT. Therefore, they received 2 treatments of 10 min PDT followed by 5 treatments of 40 min PDT (Fig. 4g, caspase-3 evaluation group). For the "Size evaluation" group, tumor size was measured using a vernier caliper one day post-PDT, and tumor volume was calculated using the formula, $V = (L \times W^2)/2$. Mice were treated repeatedly with 10 min of 980 nm irradiation PDT four times, which started to show tumor size differences on Day 8, leading to an adjustment to 40 min of PDT. Therefore, they received 4 treatments of 10 min PDT followed by 3 treatments of 40 min PDT (Fig. 4g, size evaluation group). For the caspase-3 evaluation group, the first two treatments of 10 min PDT resulted in less obvious ratiometric

NIR-IIb imaging (Fig. 4h, before treatment adjustment) and low urine Cy7.5 fluorescence intensity (Fig. 4i, before treatment adjustment). After adjusting the therapeutic plan to 40 min PDT, both the ratiometric NIR-IIb imaging (Fig. 4h, after treatment adjustment) and urine Cy7.5 fluorescence intensity (Fig. 4i, after treatment adjustment) were obviously enhanced. After two sessions of 10 min PDT and five sessions of 40 min PDT, the "customized therapy *via* caspase-3 evaluation" group demonstrated similar extents of ratiometric NIR-IIb imaging and urine Cy7.5 fluorescence values compared with the 40 min PDT treatment group (Fig. 4j). The caspase-3 evaluation group also showed effective suppression (78.9%) of tumor sizes compared with the saline-treated group after 14 days of PDT treatment (Fig. 4d, caspase-3 evaluation group and Fig. S23,† caspase-3 evaluation group). In comparison, the "customized therapy *via* tumor size evaluation" group was initially treated with 10 min of PDT for the first four sessions and showed very little size differences compared with the 40 min PDT treatment group until Day 8 (Fig. 4d, size evaluation group). Therefore, this group was adjusted to 40 min of PDT only for the last three therapeutic sessions. Due to the lack of timely treatment adjustment, the tumor size evaluation group exhibited similar growth trends to the 10 min PDT treatment group, resulting in a limited tumor-size suppression of 52.7% compared with the saline-treated group after 14 days of PDT treatment (Fig. 4d, size evaluation group and Fig. S23,† size evaluation group). Results from H&E, TUNEL, and Casp-3 I&H immunohistochemistry also showed more obvious tumor tissue apoptosis and caspase-3 expression in the caspase-3 evaluation group compared with the size evaluation group (Fig. S24†). Throughout the whole treatment period, all mice groups did not present body weight changes (Fig. S25†). These results indicate the successful implementation of customized therapy with real-time therapeutic effect evaluation, which effectively enhanced the overall therapeutic effect.

The *in vivo* biosafety and metabolism of LNPs-RB/Pep/cRGD were evaluated by injecting it into healthy mice, followed by *in vivo* imaging of NIR-IIb fluorescence under low power 980 nm irradiation (0.05 W cm^{-2}). The imaging clearly showed blood vessels after intravenous injection, indicating good systematic circulation. LNPs-RB/Pep/cRGD started accumulating in the liver, and one day post-injection, its levels gradually decreased over time due to metabolism (Fig. S26a†). The *In vivo* fluorescence of LNPs-RB/Pep/cRGD almost disappeared after eight days post-injection with 83.3% excreted in feces (Fig. S26b†), and very little amount remained in the main organs (Fig. S26c†). These results indicate that LNPs-RB/Pep/cRGD could be rapidly excreted *via* the biliary excretory pathway.[24] Major organs (heart, liver, spleen, lung, and kidney) showed no obvious damage or abnormalities in all treated mice, as confirmed by H&E staining (Fig. S27†).

3. Conclusions

We have developed a customized cancer treatment system by integrating PDT with real-time efficiency feedback capabilities to lanthanide nanoparticles. LNPs-RB/Pep/cRGD was developed and sequentially irradiated with low-power 980 nm irradiation, high power 980 nm irradiation, and 808 nm irradiation for NIR-IIb imaging-guided PDT, with real-time therapeutic effect evaluation *via* ratiometric NIR-IIb fluorescence imaging and urine NIR fluorescence measurement of caspase-3 generation. The PDT therapeutic effect was reported as early as 12 h post-treatment, which was one week earlier than the traditional method of tumor size observation. Customized treatment was performed by timely adjusting PDT duration based on real-time imaging results, effectively improving therapy results compared to adjusting PDT dosage based on tumor size changes. Therefore, the reported LNPs-RB/Pep/cRGD could provide a promising platform for efficient, customized cancer therapy for real time therapeutic efficiency evaluation. Additional excitation light could be incorporated for logically programming emission lights, which would enhance the functionality of LNPs in biomedical applications.

Author contributions

Y. Liu conceived and designed the experiments and supervised the project. H. X. Zhao, Y. Liu, W. Chen, Y. Zhu, Z. C. Chao, and J. H. Sun performed the experiments. H. X. Zhao, W. Chen, and Y. Liu analyzed the data. Q. Zhang, H. Q. Guo, and H. X. Ju provided suggestions. H. X. Zhao and Y. Liu wrote the manuscript. All authors discussed the results and commented on the manuscript.

Data availability

The data that support the findings of this study are available from the corresponding author upon reasonable request.

Conflicts of interest

The authors declare no competing financial interest.

Acknowledgements

We gratefully acknowledge the National Natural Science Foundation of China (22374073, 22022405, 21974064) and the State Key Laboratory of Analytical Chemistry for Life Science (5431ZZXM2204, 5431ZZXM2307).

References

1 F. C. Wang, N. Sun, Q. Li, J. Yang, X. Q. Yang and D. B. Liu, *J. Am. Chem. Soc.*, 2023, **145**, 919–928.
2 X. Wang, Q. Ding, R. R. Groleau, L. L. Wu, Y. T. Mao, F. D. Che, O. Kotova, E. M. Scanlan, S. E. Lewis, P. Li,

B. Tang, T. D. James and T. Gunnlaugsson, *Chem. Rev.*, 2024, **124**, 7106–7164.
3 A. Sharma, P. Verwilst, M. L. Li, D. D. Ma, N. Singh, J. Yoo, Y. Kim, Y. Yang, J. H. Zhu, H. Q. Huang, X. L. Hu, X. P. He, L. T. Zeng, T. D. James, X. J. Peng, J. L. Sessler and J. S. Kim, *Chem. Rev.*, 2024, **124**, 2699–2804.
4 D. Crosby, S. Bhatia, K. M. Brindle, L. M. Coussens, C. Dive, M. Emberton, S. Esener, R. C. Fitzgerald, S. S. Gambhir, P. Kuhn, T. R. Rebbeck and S. Balasubramanian, *Science*, 2022, **375**, 1244.
5 C. D. DiNardo and A. E. Perl, *Nat. Rev. Clin. Oncol.*, 2019, **16**, 73–74.
6 Y. X. Liu, X. J. Zhu, Z. Wei, K. F. Wu, J. F. Zhang, F. G. Mutti, H. Zhang, F. F. Loeffler and J. Zhou, *Angew. Chem., Int. Ed.*, 2023, **62**, e202303570.
7 S. S. He, J. C. Li, Y. Lyu, J. G. Huang and K. Y. Pu, *J. Am. Chem. Soc.*, 2020, **142**, 7075–7082.
8 W. Pan, M. Rafiq, W. Haider, Y. Y. Guo, H. A. Wang, M. Y. Xu, B. Yu, H. L. Cong and Y. Q. Shen, *Coord. Chem. Rev.*, 2024, **514**, 215907.
9 C. Wang, S. L. Li, B. S. Qian, J. Sun, Z. G. He, Y. Q. Wang, S. W. Zhang and C. Luo, *Coord. Chem. Rev.*, 2024, **520**, 216148.
10 S. Kataria, J. F. Qi, C. W. Lin, Z. M. Li, E. L. Dane, A. M. Iyer, J. Sacane, D. J. Irvine and A. M. Belcher, *ACS Nano*, 2023, **17**, 17908–17919.
11 N. A. Thornberry and Y. Lazebnik, *Science*, 1998, **281**, 1312–1316.
12 Y. Wang, W. Gao, X. Shi, J. Ding, W. Liu, H. He, K. Wang and F. Shao, *Nature*, 2017, **547**, 99–103.
13 Q. R. Fu, X. Yang, M. Z. Wang, K. Zhu, Y. Wang and J. B. Song, *ACS Nano*, 2024, **18**, 3916–3968.
14 P. H. Cheng, Q. Q. Miao, J. C. Li, J. G. Huang, C. Xie and K. Y. Pu, *J. Am. Chem. Soc.*, 2019, **141**, 10581–10584.
15 Q. R. Fu, H. J. Feng, L. C. Su, X. Zhang, L. T. Liu, F. F. Fu, H. H. Yang and J. B. Song, *Angew. Chem., Int. Ed.*, 2022, **61**, e202112237.
16 X. L. Huang, M. Swierczewska, K. Y. Choi, L. Zhu, A. Bhirde, J. Park, K. Kim, J. Xie, G. Niu, K. C. Lee, S. Lee and X. Y. Chen, *Angew. Chem., Int. Ed.*, 2012, **51**, 1625–1630.
17 D. J. Ye, A. J. Shuhendler, L. N. Cui, L. Tong, S. S. Tee, G. Tikhomirov, D. W. Felsher and J. H. Rao, *Nat. Chem.*, 2014, **6**, 519–526.
18 J. J. Wang, L. W. Zhang, M. L. Chen, S. Gao and L. Zhu, *ACS Appl. Mater. Interfaces*, 2015, **7**, 23248–23256.
19 C. M. Yu, L. H. Qian, J. Y. Ge, J. Q. Fu, P. Y. Yuan, S. C. L. Yao and S. Q. Yao, *Angew. Chem., Int. Ed.*, 2016, **55**, 9272–9276.
20 Y. Y. Yuan, R. T. K. Kwok, B. Z. Tang and B. Liu, *J. Am. Chem. Soc.*, 2014, **136**, 2546–2554.
21 Y. F. Wang, W. Du, T. Zhang, Y. Zhu, Y. H. Ni, C. C. Wang, F. M. S. Raya, L. W. Zou, L. S. Wang and G. L. Liang, *ACS Nano*, 2020, **14**, 9585–9593.
22 F. Wang, Y. Zhong, O. Bruns, Y. Liang and H. Dai, *Nat. Photonics*, 2024, **18**, 535–547.
23 Z. Zhang, Y. Du, X. Shi, K. Wang, Q. Qu, Q. Liang, X. Ma, K. He, C. Chi, J. Tang, B. Liu, J. Ji, J. Wang, J. Dong, Z. Hu and J. Tian, *Nat. Rev. Clin. Oncol.*, 2024, **21**, 449–467.
24 S. Wang, Y. Fan, D. Li, C. Sun, Z. Lei, L. Lu, T. Wang and F. Zhang, *Nat. Commun.*, 2019, **10**, 1058.
25 Y. Yang, C. X. Sun, S. F. Wang, K. Yan, M. Y. Zhao, B. Wu and F. Zhang, *Angew. Chem., Int. Ed.*, 2022, **61**, e202117436.
26 Y. L. Chang, H. R. Chen, X. Y. Xie, Y. Wan, Q. Q. Li, F. X. Wu, R. Yang, W. Wang and X. G. Kong, *Nat. Commun.*, 2023, **14**, 1079.
27 Y. Yang, Y. Chen, P. Pei, Y. Fan, S. Wang, H. Zhang, D. Zhao, B.-Z. Qian and F. Zhang, *Nat. Nanotechnol.*, 2023, **18**, 1195–1204.
28 Z. H. Chen, X. H. Wang, M. Z. Yang, J. Ming, B. F. Yun, L. Zhang, X. S. Wang, P. Yu, J. Xu, H. X. Zhang and F. Zhang, *Angew. Chem., Int. Ed.*, 2023, **62**, e2023118.
29 G. Y. Chen, H. L. Qju, P. N. Prasad and X. Y. Chen, *Chem. Rev.*, 2014, **114**, 5161–5214.
30 F. Q. Ren, F. F. Wang, A. Baghdasaryan, Y. Li, H. R. Liu, R. S. Hsu, C. C. Wang, J. C. Li, Y. T. Zhong, F. Salazar, C. Xu, Y. Y. Jiang, Z. R. Ma, G. Z. Zhu, X. Zhao, K. K. Wong, R. Willis, K. C. Garcia, A. Wu, E. Mellins and H. J. Dai, *Nat. Biomed. Eng.*, 2024, **8**, 726–739.
31 Z. Fang, C. Wang, J. Yang, Z. Song, C. Xie, Y. Ji, Z. Wang, X. Du, Q. Zheng, C. Chen, Z. Hu and Y. Zhong, *Nat. Nanotechnol.*, 2024, **19**, 124–130.
32 H. Li, X. Wang, T. Y. Ohulchanskyy and G. Y. Chen, *Adv. Mater.*, 2021, **33**, 2000678.
33 J. T. Xu, A. Gulzar, P. P. Yang, H. T. Bi, D. Yang, S. L. Gai, F. He, J. Lin, B. G. Xing and D. Y. Jin, *Coord. Chem. Rev.*, 2019, **381**, 104–134.
34 N. Liao, L. Su, Y. Zheng, B. Zhao, M. Wu, D. Zhang, H. Yang, X. Liu and J. Song, *Angew. Chem., Int. Ed.*, 2021, **60**, 20888–20896.
35 T. Chen, P. D. Hou, Y. F. Zhang, R. J. Ao, L. C. Su, Y. F. Jiang, Y. L. Zhang, H. L. Cai, J. Wang, Q. S. Chen, J. B. Song, L. S. Lin, H. H. Yang and X. Y. Chen, *Angew. Chem., Int. Ed.*, 2021, **60**, 15006–15012.
36 P. Pei, H. Hu, Y. Chen, S. Wang, J. Chen, J. Ming, Y. Yang, C. Sun, S. Zhao and F. Zhang, *Nano Lett.*, 2022, **22**, 783–791.
37 M. Y. Zhao, B. H. Li, Y. F. Wu, H. S. He, X. Y. Zhu, H. X. Zhang, C. R. Dou, L. S. Feng, Y. Fan and F. Zhang, *Adv. Mater.*, 2020, **32**, 2001172.
38 C. L. Wang, H. X. Lin, X. G. Ge, J. Mu, L. C. Su, X. Zhang, M. Niu, H. H. Yang and J. B. Song, *Adv. Funct. Mater.*, 2021, **31**, 2009942.
39 D. Song, C. C. Li, M. T. Zhu, S. Y. Chi and Z. H. Liu, *Angew. Chem., Int. Ed.*, 2022, **61**, e2022127.
40 Y. Zhong, Z. Ma, S. Zhu, J. Yue, M. Zhang, A. L. Antaris, J. Yuan, R. Cui, H. Wan, Y. Zhou, W. Wang, N. F. Huang, J. Luo, Z. Hu and H. Dai, *Nat. Commun.*, 2017, **8**, 737.
41 H. X. Zhao, Y. T. Li, X. B. Zhang, K. Wu, J. H. Lv, C. Chen, H. P. Liu, Z. Z. Shi, H. X. Ju and Y. Liu, *Biomaterials*, 2022, **291**, 121873.

42 A. Srivatsan, M. Ethirajan, S. K. Pandey, S. Dubey, X. Zheng, T. H. Liu, M. Shibata, J. Missert, J. Morgan and R. K. Pandey, *Mol. Pharm.*, 2011, **8**, 1186–1197.
43 Y. L. He, S. W. Guo, Y. Zhang, Y. Liu and H. X. Ju, *Biomaterials*, 2021, **275**, 120962.
44 L. Faleiro and Y. Lazebnik, *J. Cell Biol.*, 2000, **151**, 951–959.
45 S. Kamada, U. Kikkawa, Y. Tsujimoto and T. Hunter, *J. Biol. Chem.*, 2005, **280**, 857–860.
46 Y. Chen, P. Pei, Y. W. Yang, H. X. Zhang and F. Zhang, *Angew. Chem., Int. Ed.*, 2023, **62**, e2023016.
47 M. Z. Xu, Y. M. Qi, G. S. Liu, Y. Q. Song, X. Y. Jiang and B. J. Du, *ACS Nano*, 2023, **17**, 20825–20849.